Palacký University Olomouc
Faculty of Science

Department of Optics

Homodyne detection for characterization of coherent-state thermalization

Bachelor's Thesis

Martin Dostál

Palacký University Olomouc
Faculty of Science

Department of Optics

Homodyne detection for characterization of coherent-state thermalization

Bachelor's Thesis

Author:	Martin Dostál
Study programme:	B1701 Physics
Field of study:	Optics and Optoelectronics
Form of study:	Full-time
Supervisor:	RNDr. Miroslav Ježek, Ph.D.
Co-supervisor:	Mgr. Jan Bílek, Ph.D.

Thesis submitted on: . . . .

Univerzita Palackého
Přírodovědecká fakulta

Katedra optiky

Charakterizace procesu termalizace koherentních stavů pomocí homodynní detekce

Bakalářská práce

Autor:	Martin Dostál
Studijní program:	B1701 Fyzika
Studijní obor:	Optika a optoelektronika
Forma studia:	Prezenční
Vedoucí:	RNDr. Miroslav Ježek, Ph.D.
Co-supervisor:	Mgr. Jan Bílek, Ph.D.

Práce odevzdána dne: . . . .

Abstract

Homodyne detection is a powerful tool used in many fields of optics such as optical communications and metrology. This work aims at quantum homodyne detection, which is widely used in quantum optics for the measurement of quantum states. Here we perform the detailed characterization of a time-resolved quantum homodyne detector and demonstrate its balancing and calibration.

The homodyne detection is applied to the characterization of coherent state thermalization. The single-mode thermal light can be emulated by the interference of many coherent states with random phases. We show the dynamic of the transition between coherent and thermal states by mixing two and four coherent states and perform the homodyne measurement of the resulting states

i

Contents

Chapter 1

Introduction

Homodyne detection is a measurement method widely used in many fields of optics. The most important application is in optical communications [1, 2, 3], where is used for measuring signals with phase or quadrature-amplitude modulation. Another important application of homodyne detection is optical metrology. A special form of homodyne detection is quantum homodyne detection used for the observation of quantum states such as squeezed states. This can be used in quantum cryptography and basic research such as gravitational-wave detection [4], or elsewhere where we need to work with well-defined quantum states.

Unlike other methods such as detectors using one photodiode or charge-coupled devices, homodyne detection offers the possibility to measure phase information of an unknown signal [5]. The phase information is obtained by comparing the measured signal with a reference signal (local oscillator), which allows measuring the relative phase between these signals. This method can be used with arbitrary optical or RF signals. In homodyne detection, the measured signal and the local oscillator have the same frequency. For this reason, it is convenient to use the same light source for both signals.

The measured signal and the local oscillator interfere at the beam splitter and the high quantum efficiency photodiodes detect the output signals. For balanced homodyne detection, the mean values of the photocurrent from the photodiodes are the same. We get the signal from the detector by subtracting the signals from photodiodes. Since the signal from homodyne detection is weak, the amplifier is an important part of homodyne detection. The noise of the amplifier must be lower than the noise of the signal. For this reason, we can use only a few suitable amplifiers, especially in a time domain. There are two types of amplifiers mostly used for homodyne detection, transimpedance amplifiers and charge sensitive amplifiers. In this work, we use a charge sensitive amplifier, first employed for quantum homodyne detection by Hansen et al. [6].

There are two basic modes of homodyne detection, the frequency domain where the local oscillator and signal are obtained from continuous-wave sources, and the time domain, where the local oscillator and signal are obtained from pulsed sources. The homodyne detection in the frequency domain can be used for the measurement of coherent, vacuum and squeezed states of light, which can be used, for example, for optical communications. On the other hand, nontrivial quantum states are usually generated in the time domain [7, 8]. However, ho-

modyne detection in pulse mode is extremely experimentally challenging. The most important is the bandwidth of the detector, which is given by the response of photodiodes and the cut-off frequency of the amplifier. This frequency must be higher than the repetition frequency of the laser source. Typically, there is a trade-off between the cutoff frequency and signal-to-noise ratio (SNR) of the amplifier.

Optical homodyne detection was first used for the measurement in the frequency domain [9]. The first quantum time-domain homodyne detection was performed in 1993 by Raymer et al. [5]. The homodyne detector was used for the measurement of the Wigner distribution of the vacuum state and the squeezed state. Hansen et al. in 2001 [6] used charge sensitive amplifier for amplifying the signal from the homodyne detector for the first time. The homodyne detector had a cutoff frequency higher than 1 MHz with SNR 14 dB and was used for the reconstruction of the single-photon fock state. The homodyne detector with a cutoff frequency of 250 MHz was designed by Okubo et al. [10] in 2008, but the SNR was only 7.5 dB and the detector was unstable. In 2009 Haderka et al. [11] used transimpedance amplifier for homodyne detection; the detector had a cutoff frequency of 54 MHz and SNR 12 dB. The detectors designed by Zavatta et al. [12] in 2011, Kumar et al. [13], and Cooper et. al [14] in 2012 can be used for detecting signals from most commercially available mode-locked lasers.

For the full reconstruction of the quantum coherent states from homodyne measurements, we use a procedure called homodyne tomography. The arbitrary quantum state can be described by the density operator $\hat{\rho}$ or by the quasiprobability distribution in phase space called the Wigner function. Assume that we observe an unknown quantum state via homodyne detection. The measured data will form statistics, which corresponds to a marginal distribution of the unknown state along an axis determined by the relative phase between the local oscillator and the measured signal. We perform many measurements with different relative phases and from obtained data we can reconstruct the unknown state. With an increasing number of measurements, we can reconstruct the state more precisely. The different methods of homodyne tomography are reviewed by Lvovsky and Raymer in [15].

Thermal sources are the major sources of natural light. The radiation of these sources can be approximated by the black body radiation. This radiation is incoherent with a continuous frequency spectrum, which density is described by Planck's law. When we filter out a single mode from a thermal source, it possesses the Bode-Einstein photon statistics. On the other hand, the most simple model of light emission known from the theory of electromagnetic field is an oscillating electric dipole emitting monochromatic and coherent light with Poissonian statistics. We assume, that the black body is composed of many such dipoles, while each dipole emits coherent light (coherent state) with random frequency and phase. Thus single-mode thermal light (thermal state) is formed by interference of many coherent states with random phases. A coherent state thermalization is a transition between coherent and thermal light. We can study the thermalization for only a few interfering coherent states to explore the transition in detail.

This work will focus on the homodyne detector characterization and the measurement of the coherent state thermalization. In Chapter 2, the basic theory of homodyne tomography, the maximum likelihood estimation method, and the thermalization process will be presented. We will define the quantum

states used in the work such as vacuum state, coherent state, and thermal state. We will also show their decomposition into the basis of Fock states. In Chapter 3, we will propose a method for selecting suitable photodiodes for the homodyne detector and we will show the dependence of the photodiode time response shape on the bias voltage. Furthermore, we will characterize the electronic spectrum of the homodyne detector and the dependence of the noise variation on the power of the local oscillator. We will also describe the balancing process of the detector and its calibration. In Chapter 4, the setup of the thermalization experiment will be described in detail. We will show the main problems of the adjustment of the setup and its characterization. Finally, the results of the coherent state thermalization and their comparison with the simulations will be presented.

Chapter 2

Basic concepts

2.1 Homodyne detection

To get a better idea of the fundamentals of homodyne detection, let us show the homodyne detection for a classical coherent state as local oscillator. This can be in phase space (x, p) described by complex number a, or by quadrature amplitudes X and P given by

$$X = \frac{1}{\sqrt{2}}(a + a^*), \tag{2.1}$$

$$P = \frac{1}{i\sqrt{2}}(a - a^*). \tag{2.2}$$

Sometimes is more convenient to describe the position of the state by a mean photon number $\bar{n}$ (or intesity I) and optical phase ϕ. These are given by

$$\bar{n} = I = |a|^2 \tag{2.3}$$

$$\phi = \arctan \frac{P}{X}. \tag{2.4}$$

If we consider the free evolution of the mode, the coherent state oscillates as

$$a = a_0 e^{i\omega t}, \tag{2.5}$$

where $\omega/2\pi$ is the frequency of the oscillations. This frequency is for visible light in the hundreds of THz, which is typically impossible to measure with electronic detectors. For this reason, we can only measure the relative phase between two states of light. We can define a rotated quadrature X_θ given by

$$X_\theta = \frac{1}{2}(e^{-i\theta}a + e^{i\theta}a^*), \tag{2.6}$$

where θ is the relative phase.

In homodyne detection, we have the coherent reference state (local oscillator) β with intensity I_β, and the measured state (signal) α with intensity I_α, with relative phase between them θ. These states are mixed at a beam splitter with transmittance T and reflectance R. The interaction provided by the beam
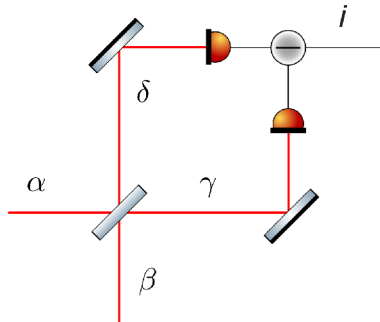
Figure 2.1: The scheme of the homodyne detection.

splitters is given as

$$\begin{pmatrix} \gamma \\ \delta \end{pmatrix} = \begin{pmatrix} \sqrt{T} & \sqrt{R} \\ -\sqrt{R} & \sqrt{T} \end{pmatrix} \begin{pmatrix} \alpha \\ \beta \end{pmatrix} \qquad (2.7)$$

The output states γ and δ are converted into electrical signals by the photodiodes. We get the resulting signal i by subtracting these signals from each other. The scheme of homodyne detection can be seen in Fig. 2.1. The signal i will be given as

$$i = (I_\alpha - I_\beta)(T - R) + 4\sqrt{R \cdot T \cdot I_\alpha} X_\theta. \qquad (2.8)$$

For the beam splitter 50:50, $T = R = 1/2$, and the detected current i is given by

$$i = 2\sqrt{I_{\mathrm{LO}}} X_\theta. \qquad (2.9)$$

However, in the full quantum description, the state in the phase space is given by the probability density distribution. Due to that, we have to replace quadrature amplitudes X and P with quadrature operators $\hat{X}$ and $\hat{P}$ given by

$$X = \frac{1}{\sqrt{2}}(\hat{a} + \hat{a}^\dagger), \qquad (2.10)$$

$$P = \frac{1}{i\sqrt{2}}(\hat{a} - \hat{a}^\dagger), \qquad (2.11)$$

where $\hat{a}^\dagger$ and $\hat{a}$ are bosonic creation and annihilation operators, $[\hat{a}, \hat{a}^\dagger] = 1$. The commutation between quadrature operators is then $[\hat{X}, \hat{P}] = i$ and uncertainty relations are

$$\Delta \hat{X} \Delta \hat{P} \geq \frac{1}{4}. \qquad (2.12)$$

The final equation for the detected current can be derived from the classical case as

$$\hat{i} = 2\sqrt{I_{\mathrm{LO}}} \hat{X}_\theta. \qquad (2.13)$$

As we can see, the measured signal depends only on the local oscillator amplitude and on the relative phase θ between the signal and the local oscillator. For this reason, the power of the local oscillator has to be as high as possible for the highest SNR. However, there is the power of the local oscillator has to be lower than the power, which saturates the homodyne detector. Homodyne detection

allows us to measure the quantum state probability distribution in phase space along an axis whose direction is given by θ. It follows that the quantum state can be reconstructed from many measurements with different θ, where the number of measurements determines the resolution of the reconstructed state. Thus we need many copies of the measured quantum state. For the measurement of classical quantum states following the Gaussian probability density distribution we need at least two measurements along different axes. This can be done by two measurements using a single homodyne detector, or one measurement using two distinct homodyne detectors. In this work, we use the first approach. The procedure of reconstructing the quantum states from the homodyne data is called homodyne tomography.

2.2 Quantum states

In quantum optics, there are several basic quantum states. The first and most important is the vacuum state. If we consider that light can be approximated by the linear harmonical oscillator model, the vacuum state has the lowest possible energy, but this energy is non-zero. This can be possible due to uncertainty relations between $\hat{X}$ and $\hat{P}$. The vacuum state is also symmetric about the origin of the phase space. Due to this, the other states can be created by injecting photons into this state or displacing it from the origin of the phase space. The vacuum state is important for calibrating the homodyne detector. Since the variance of the vacuum state is the lowest possible and its mean amplitude in phase space is zero (see Fig. 2.2 A), we can assume, that the vacuum state has the same Gaussian probability distribution along all axis with a variance of $\frac{1}{2}$ and a mean value of 0.

The Fock states are quantum states with an exactly defined number of particles (photons). The probability distribution of Fock state $|1\rangle$ in phase space is shown in Fig. 2.2 B. This single-photon state can be used in quantum computing or quantum cryptography. In this work, we use a Fock representation of quantum states for their characterization; it corresponds to the photon-number distribution. This distribution can be described by the moments such as the mean photon number (the first moment) and the variation (the second central moment).

Coherent states are eigenstates of the linear harmonic oscillator. In the phase space, their variance is the same as the vacuum state and their amplitude depends on their energy (see Fig. 2.2 C). In the Fock basis, the coherent state has a Poisson distribution (see Fig. 2.3 A) given as

$$f(n) = \frac{\bar{n}^n e^{-\bar{n}}}{n!}, \tag{2.14}$$

where $\bar{n}$ is the mean photon number. For the Poisson distribution, the variance of the distribution is the same as the mean photon number. The coherent state was first proposed by Erwin Scrödinger in 1926. From the electromagnetic field theory, a coherent wave is emitted by the oscillating electric dipole. The laser light can be considered coherent with good approximation.

Thermal light is produced by the radiation of the black body with temperature T. In our case, the temperature is represented by the mean photon number $\bar{n}$. In the phase space, the thermal state variation is greater than the variation
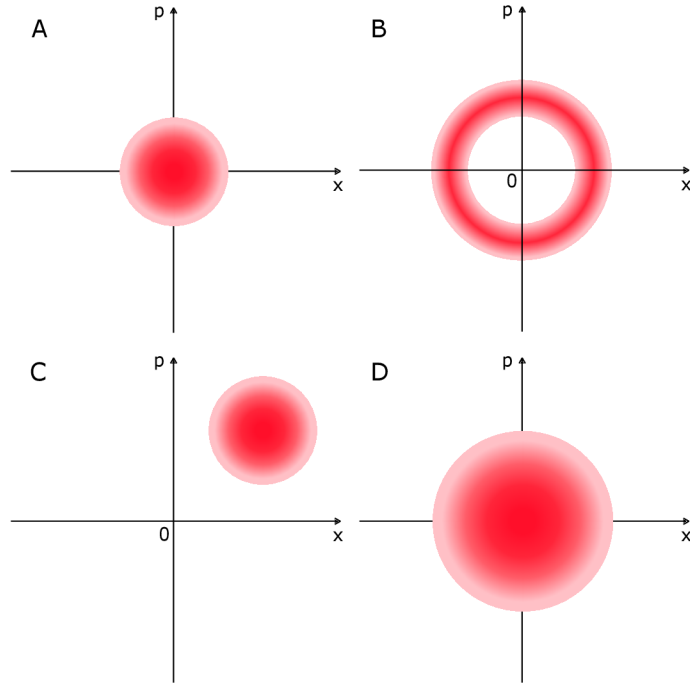
Figure 2.2: (A) The vacuum state probability distribution in the phase space. (B) The Fock state probability distribution in the phase space. (C) The coherent state probability distribution in the phase space. (D) The thermal state probability distribution in the phase space.
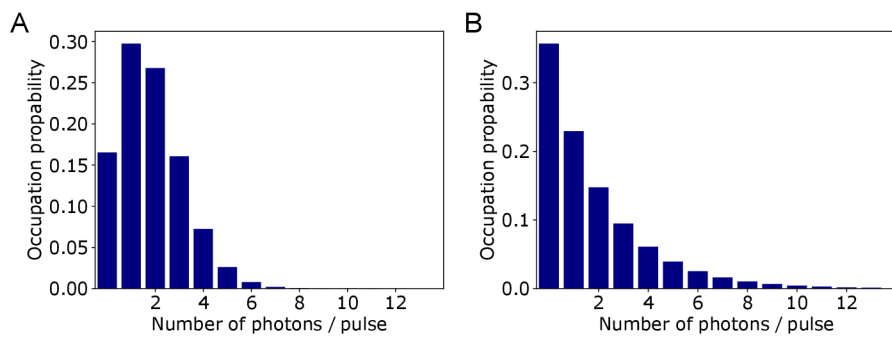

Figure 2.3: (A) The theoretical photon number distribution of the coherent state. (B) The theoretical photon number distribution of the thermal state. Both distributions are for $\bar{n} = 1.8$

of the vacuum state and its amplitude is zero (see Fig. 2.2 D). The thermal state for the temperature 0 K is the vacuum state. The distribution in the Fock basis is the Bose-Einstein statistics (see Fig. 2.3 B) given as

$$f(n) = \frac{\bar{n}^n}{(\bar{n}+1)^{n+1}}.$$ (2.15)

2.3 Coherent state thermalization

Photon statistics, i.e. the probability distribution of various numbers of photons in a quantum state of light, is a fundamental characteristic of optical signals. As said above, the single-mode thermal state can be achieved by the interference of many coherent states of light with random phases. Thus, in the limit of infinitely many coherent states, the resulting superposition signal is indistinguishable from a single-mode thermal state. The photon statistics of the coherent state follows the Poissonian distribution and the photon statistics of the single-mode thermal state follows the Bose-Einstein distribution. In the coherent state thermalization, we want to explore the photon statistics of the states between those two extremes. To this end, we measured the photon statistics of the coherent state, interference of two phase-randomized coherent states (1st thermalization stage) and interference of four phase-randomized coherent states (2nd thermalization stage) by homodyne detection. For the preparation of these states, we had four coherent states, which we pair-wise interfered at beam splitters (see Fig. 2.4).
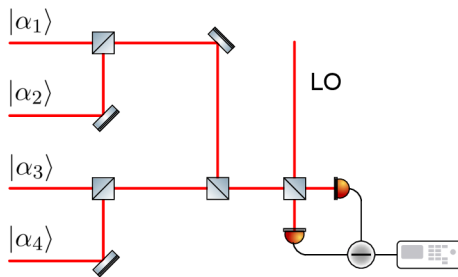

Figure 2.4: The scheme of the coherent state thermalization.

We compared measured statistics with theoretical ones. As said above, for one coherent state, the photon statistics follow the Poissonian distribution. The other photon statistics we obtained with theoretical simulations performed using the Python programming language and Qutip library. We created mathematical models of two coherent states with random phases, $|\alpha_1\rangle$ and $|\alpha_2\rangle$. These states are mixed on the 50:50 beam-splitter. Output states can be described in the Heisenberg representation by relation

$$\hat{\rho}_{12,\text{out}} = \hat{U}\hat{\rho}_{12,\text{in}}\hat{U}^\dagger$$ (2.16)

where $\hat{\rho}_{12,\text{out}}$ is a density operator of output state given as $\hat{\rho}_{12,\text{out}} = |\alpha_1, \alpha_2\rangle\langle\alpha_1, \alpha_2|$. $\hat{U}$ is evolution operator given by $\hat{U}(\phi) = e^{-i\phi\hat{H}}$, where $\phi = \frac{\pi}{2}$ for beam-splitter

50:50 and $\hat{H}$ is Hamiltonian of the beam-splitter given by

$$\hat{H} = \frac{i}{2}(\hat{a}_1^\dagger \hat{a}_2 - \hat{a}_1 \hat{a}_2^\dagger), \qquad (2.17)$$

where $\hat{a}_1$ and $\hat{a}_2$ are annihilation operators of the first and second modes, respectively. The resulting output states $\hat{\rho}_{\text{out}}$ can be obtained as the partial traces of $\hat{\rho}_{12,\text{out}}$, $\hat{\rho}_{\text{out}} = \text{Tr}_2[\hat{\rho}_{12,\text{out}}]$. Higher thermalization stages can be obtained by repeating this process. Instead of the coherent states, we brought on the beam-splitter input states from the first thermalization stage for the preparation of the second thermalization stage state, and so on.

For the description of the photon statistics, we used the mean photon number $\bar{n}$, the variance $\text{Var}(n)$ and the parameter $g^{(2)}(0)$. The $g^{(2)}(\tau)$ is a degree of second-order coherence given as

$$g^{(2)}(\tau) = \frac{\langle I(t)I(t+\tau)\rangle}{\langle I(t)\rangle^2}, \qquad (2.18)$$

where I is the intensity of the signal. For our needs, we consider $\tau = 0$, hence the parameter can be calculated as

$$g^{(2)} = 1 + \frac{\text{Var}(n)^2 - \bar{n}}{\bar{n}^2}, \qquad (2.19)$$

where n is the photon number. For the Poissonian distribution $\text{Var}(n) = \bar{n}$, and for Bose-Einstein distribution $\text{Var}(n) = \bar{n}(\bar{n}+1)$. Thus for the ideal coherent state $g^{(2)} = 1$ and for the thermal state $g^{(2)} = 2$.

2.4 Maximum likelihood estimation

Maximum likelihood estimation (MaxLik) is the statistical method used for the estimation of parameters of a joint probability distribution of the set of independent random variables. In quantum optics, the MaxLik is used for the reconstruction of a density matrix of the unknown quantum state from the measured data set. In other words, we want to assign to the measured data set a density matrix $\hat{\rho}_{\text{est}}$ as similar as possible to the density matrix $\hat{\rho}$ of the measured quantum state. This is similar to linear regression, where we want to estimate a model that fits the measured data as much as possible, but the problem is highly nonlinear in this case. The mathematical formulation of the MaxLik for quantum state reconstruction is developed in [16, 17, 18]. Let us assume a finite number n of identical copies of unknown state. The probabilities of individual outcomes of a measurement are $p_l(\hat{\rho}) = \text{Tr}[\hat{\rho}\hat{\Pi}_l]$, where $\hat{\Pi}_l$ are positive operator-valued measure elements. Let $f_l = k_l/n$ be the relative detection frequencies where k_l are occurrences of the outcomes $\hat{\Pi}_l$. The density operator $\hat{\rho}_{\text{est}}$ is given as

$$\hat{\rho}_{\text{est}} = \arg\max_\rho \mathcal{L}(f_l, p_l), \qquad (2.20)$$

$$\mathcal{L}(f_l, p_l) = \sum_l f_l \ln(p_l) - \lambda \text{Tr}[\hat{\rho}], \qquad (2.21)$$

where λ is a Lagrange multiplicator. The function $\mathcal{L}(f_l, p_l)$ represents the distance between the probability distribution p_l and the relative frequencies f_l. To

maximize the likelihood functional, we have to formulate a nonlinear extremal operator equation for the density matrix $\hat{\rho}$

$$\hat{\rho} = \hat{R}\hat{\rho}\hat{R}, \ \hat{R} = \sum_l \frac{f_l}{p_l}\hat{\Pi}_l, \tag{2.22}$$

which preserves the positive semidefinitness and normalization of the density operator $\hat{\rho}$. From this equation, we get an iteration algorithm

$$\hat{\rho}^{(n+1)} = \hat{R}^{(n)}\hat{\rho}^{(n)}\hat{R}^{(n)}, \tag{2.23}$$

where we can choose the initial form of the density matrix $\hat{\rho}^{(0)} = \hat{\mathbb{1}}$. Each iteration of this algorithm will monotonically increase the likelihood of the estimated density matrix to the measured one.

For homodyne detection, the probability of detecting a particular quadrature y for a given relative phase θ is

$$p(y) = \text{Tr}[\hat{\Pi}(\theta, y)\hat{\rho}], \tag{2.24}$$

where $\hat{\Pi}(\theta, y) = |\theta, y\rangle\langle\theta, y|$ is the projection onto this quadrature eigenstate, which can be in Fock basis expressed as

$$\Pi_{\text{mn}}(\theta, x) = \langle m|\theta, y\rangle\langle\theta, y|n\rangle. \tag{2.25}$$

Chapter 3

Homodyne detector operation and characterization

3.1 Homodyne detector construction and photodiodes time response

Quantum homodyne detection requires a homodyne detector with the SNR as high as possible. We also need a bandwidth higher than the laser pulse repetition rate. To this end, the components we use must be suitable for high frequencies with low noise. In this work, we used a homodyne detector with charge sensitive amplifier designed by Hansen et al. [6] and modified by M. Ježek. For the construction of the detector, we used two Hammamatsu S3883 PIN diodes, charge sensitive preamplifier AMPTEK A250, and two amplifiers AMPTEK A250. The scheme of the detector is shown in Fig. 3.1.

For the most balanced homodyne detector, we must choose two photodiodes with time responses as similar as possible. As said above in the detector used in this work, we use Hamamatsu S3883 PIN photodiodes, which are widely used in quantum homodyne detectors and provide the best trade-off of quantum efficiency and frequency response. The radius of the active area of these diodes is 1.5 mm, the quantum efficiency is 92.2 % at the wavelength of 780 nm.

Time response characterizes the dependence of the electronic signal from the photodiode on the measured optical signal. For the ideal photodiode, the electronic signal is the same as the optical one, but for a real photodiode, the electronic signal can be deformed due to the nonzero response time. This effect can be affected by the bias voltage U_{bias} applied to the photodiode, which can change the shape of the time response. We put the photodiode in the testbed for this measurement, shown in Fig. 3.2. For a better understanding of how the time response depends on the U_{bias}, we performed the measurement of the time responses of the pulsed laser signal for the different bias voltages (see Fig. 3.3 A). From measured time responses we find the area under the pulses and then compared these areas with the bias voltages (see Fig. 3.3 B).

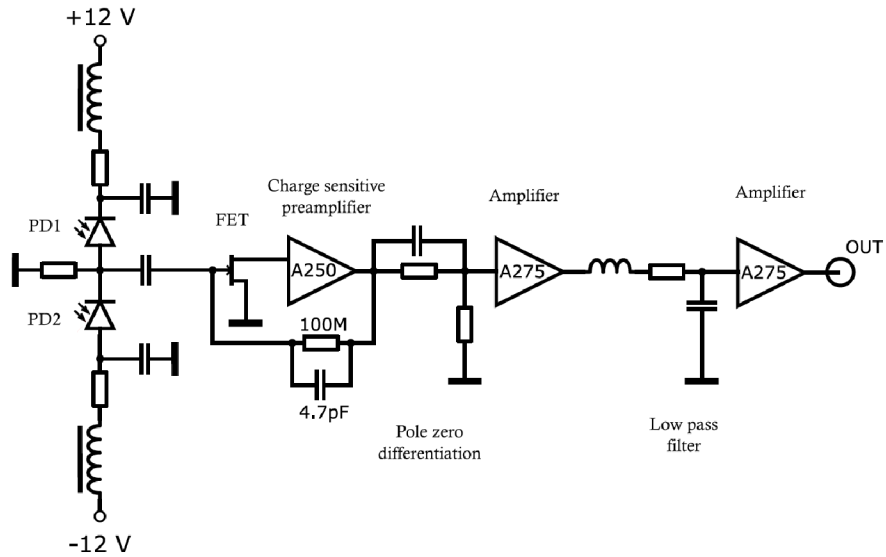We had a batch of 10 photodiodes, from which we had to select two with the

Figure 3.1: The simplified electronic scheme of the homodyne detector. The signals from photodiodes PD1 and PD2 are subtracted and brought to the input of the charge-sensitive preamplifier. We use several low-pass filters to reduce noise from external noise.
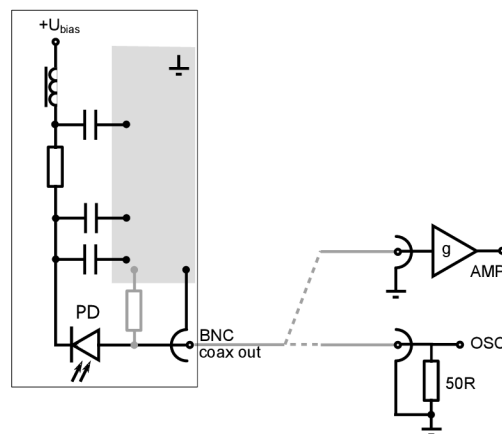

Figure 3.2: The scheme of the testbed for the photodiodes characterization. The bias voltage U_{bias} is brought to the photodiode PD through a series of low-pass filters. The signal is displayed on the oscilloscope OSC.
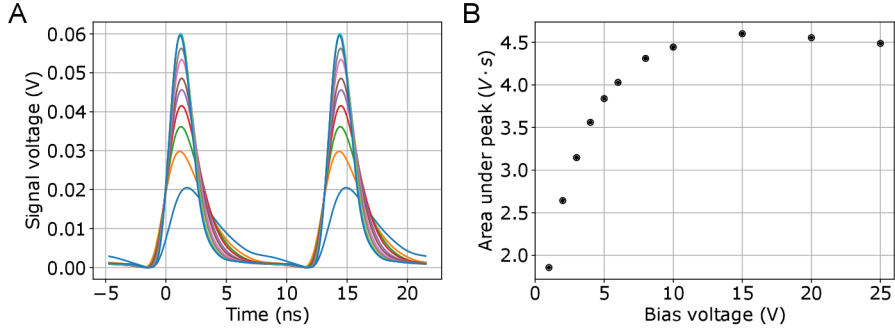
Figure 3.3: (A) The time responses for all bias voltages. (B) Dependence of the area under the pulse on the bias voltage.
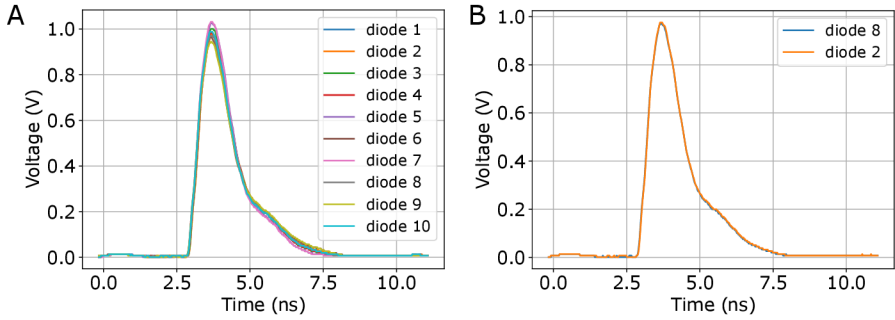

Figure 3.4: (A) The time responses for all photodiodes. (B) The corrected time responses of two chosen photodiodes.

most similar time responses. We performed the characterization for two values of U_{bias}, 20 V and 25 V. As the light source, we used a pulsed signal from a titanium–sapphire laser Mira Optima 900-F. Signal power was set to 0.488 mW at wavelength 800 nm. The output of the testbed was displayed on the oscilloscope LeCroy WavePro 715Zi. Measured traces from the oscilloscope for each photodiode can be found in Fig. 3.4. In our scheme of balanced homodyne detection, we could use several possible degrees of freedom to balance the photocurrent passing through photodiodes and the delay between pulses impinging both photodiodes. For this reason, we could consider two free parameters D and G, for which we search the global minimum O_{min} of the function

$$O = \int_0^T \left| \Delta_1^2 + \Delta_2^2 \right| dt, \tag{3.1}$$

which characterizes the overlap of time responses for both values of U_{bias}. The parameters Δ_1^2 and Δ_2^2 are the overlaps for $U_{\mathrm{bias,1}} = 20\,\mathrm{V}$ and $U_{\mathrm{bias,2}} = 25\,\mathrm{V}$; their values are given by

$$\Delta_n^2 = (U_{\mathrm{A},n}(t) - G_n \cdot U_{\mathrm{B},n}(t + D_n))^2. \tag{3.2}$$

13

We find the $O_{\min}$ for all pairs (A, B) of photodiodes. The pair with the lowest value of $O_{\min}$ was the best pair with the most similar time responses. For the measured samples, it was diode numbers 2 and 8. The time responses of these photodiodes with the correction for parameters D and G are plotted in Fig. 3.4(b).

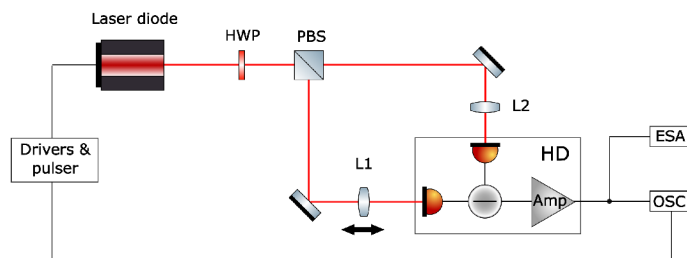## 3.2 Electronic spectrum and balancing of the homodyne detector

Figure 3.5: Scheme of the setup for balancing and characterization of the homodyne detector. The optical signal from the laser diode with polarization controlled by the half-wave plate HWP is brought to the input of the polarizing beam-splitter PBS. Outputs of PBS are brought to the inputs of homodyne detector HD. The output from HD is displayed on the oscilloscope OSC and electronic spectrum analyser ESA.

It is crucial for homodyne detection to balance the detector as much as possible. For the balancing and characterization of the homodyne detector, we used an optical setup with the local oscillator at the first port of the beam splitter and a vacuum state o the second port. The scheme of the optical setup is in Fig. 3.5. There are several degrees of freedom used to balance the detector in our optical setup. The first was a half-wave plate before the polarization beam splitter, which can optimize signal power distribution. The second is the lens in Z–axis mount, which can change the focus of the laser beam to one of the photodiodes. The last degree of freedom is the bias voltage of the photodiodes.

To determine the degree of balance of the detector we used two methods. The first uses the oscilloscope and the second uses the spectrum analyzer. After we connected the unbalanced detector output to the oscilloscope we could see unipolar laser pulses envelope, which we want to decrease so that only quantum noise remains. The difference between the unbalanced and balanced detector signals is shown in Fig. 3.6. This method we use only for primary balancing, for the final balancing we connected the output to the frequency spectrum analyzer. If the detector is unbalanced there is a peak in the frequency spectrum of the detector at the repetition frequency and its harmonics. For the best possible balanced homodyne detection, we must minimalize these peaks as much as possible. We perform the measurement of the electronic spectrum of the balanced homodyne detector for local oscillator power $10\,\mu\mathrm{W}$, the unbalanced homodyne detector for local oscillator power $0.05\,\mu\mathrm{W}$, and the homodyne detector with-

out the local oscillator, which represents electronic noise. Measured electronic spectrums are shown in Fig. 3.7. We compensated the difference between powers of the local oscillator for better comparison of electronic spectrums of the balanced and unbalanced homodyne detector. The CMRR of the first peak of the unbalanced homodyne detector electronic spectrum is 45 dB.
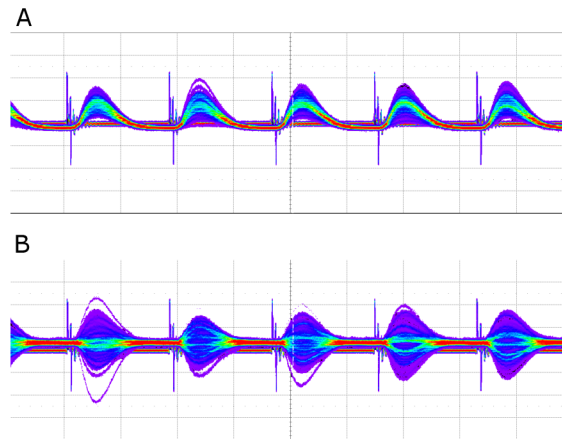

Figure 3.6: (A) The signal from the unbalanced homodyne detector. (B) The signal from the balanced homodyne detector. In the background of the signal trace is the trigger trace. For a clearer display of the signal, we used the persistency mode of the oscilloscope.
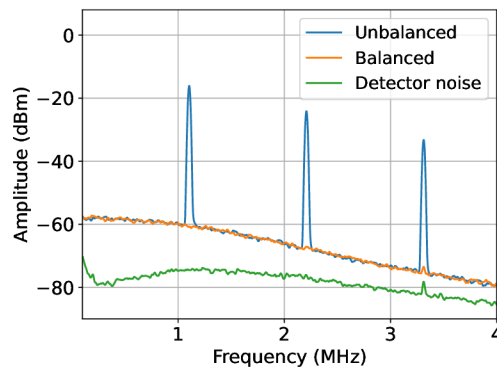

Figure 3.7: Electronic spectrum of the signal from the balanced and unbalanced homodyne detector. The CMRR for the first peak of the spectrum of the unbalanced detector is 45 dB.

3.3 Linearity and calibration of homodyne detector

As said above, homodyne detection allows us to measure the rotated quadrature $\hat{X}(\theta)$. The one rotated quadrature is given by the area under the homodyne detection signal for the time of one pulse for the homodyne detection in the time domain. The positions of pulses are given by the trigger signal from the driver switching the laser diode. The number of measured quadratures depends on the acquisition time of the oscilloscope and the repetition rate of the pulses. In this work, we obtain several thousand quadratures for one run of the measurement. We can construct a histogram of measured quadratures and calculate their variance and mean value.
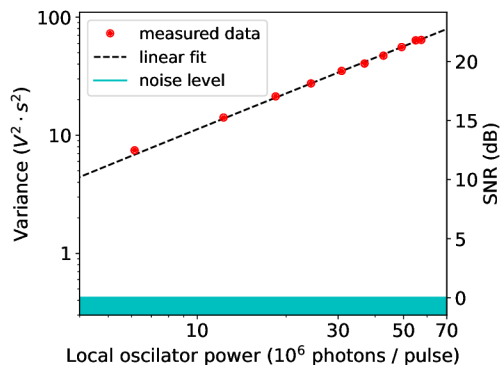

Figure 3.8: Dependence of the quadrature variance on the power of the local oscillator in LogLog scale. The measured variances are fitted by a linear function with direction 1.135.

As said in Chapter 2, the signal from the homodyne detector depend on the power of the local oscillator. To this goal, we measured the dependence of the quadratures variance (and SNR) on the power of the local oscillator for vacuum state (see Fig. 3.8). The graph shows a region from 6 million photons/pulse to 55 million photons/pulse, where the dependence is linear. For the power smaller than 6 million photons/pulse, the measured shot noise is close to the electronic noise of the detector. Nonlinearity for the power larger than 55 million photons/pulse is probably caused by imperfect balancing or saturation of the operational amplifier in the detector. For the next measurements, we need to choose the local oscillator power, which is in the linear region and at the same time is strong enough. After considering these conditions, we choose the local oscillator power of 41 million photons/pulse (10μW). This local oscillator power corresponds to the SNR higher than 20 dB.

For calibration of the detector, we used the vacuum state, which is easy to prepare and its probability distribution is the same along all axis. The quadrature distribution of the vacuum state follows the Gaussian distribution. The measured quadratures and their histogram can be found in Fig. 3.9. We fitted the histogram of the measured quadratures with the Gaussian function of

16

the form

$$\psi(x) = \frac{1}{\sigma\sqrt{2\pi}} e^{-\frac{(x-\mu)^2}{2\sigma}}, \qquad (3.3)$$

which is a probability density function of the Gaussian distribution with variance σ^2 and mean value μ. For the vacuum state $\sigma^2 = \frac{1}{2}$. The variance is given as a sum of the different noises, which include mainly the vacuum noise, but also the noise of the detector and light source. The mean value of the vacuum state is 0 by the definition, but there can be some offset caused by an offset of the operational amplifier. The variance and the mean value of the measured quadratures were $\sigma^2 = 323$ and $\mu = 21$. Actual values of both parameters are affected by the amplifier gain, its response, and also the data postprocessing. We compensate the offset and rescale the noise of the vacuum state. The calibrated quadratures are given as

$$\psi'(x) = \frac{\psi(x) - \mu}{\sigma}. \qquad (3.4)$$

The calibrated quadratures possess the variance $\sigma^2 = \frac{1}{2}$ and the mean value $\mu = 0$.
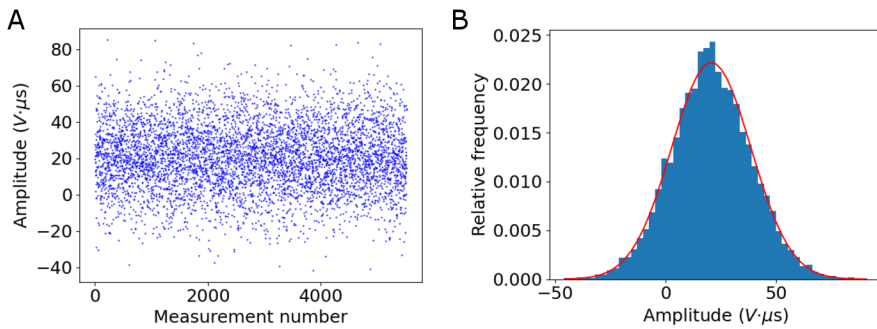

Figure 3.9: The measured quadratures (A) and the quadrature histogram (B) from the balanced homodyne detector. The variance and the mean value are $\sigma^2 = 323$ and $\mu = 21$.

Chapter 4

Thermalization of coherent states

4.1 Thermalization setup and its adjustment

The scheme of the setup we used for coherent state thermalization is shown in Fig. 4.1. As an optical source (LASER), we used the QFLD-810-10S laser diode manufactured by Q-Photonics and switched by a homemade electronic pulser, emitting nanosecond pulses with a repetition frequency of 1.1 MHz at a wavelength 808 nm. We placed a 3 nm bandpass filter after the light source for the well-defined wavelength and spectrum. The laser light is split into four signal paths $|\alpha_n\rangle$ and the local oscillator path (LO). The optical power of these paths is controlled via half-wave plates (HWP), polarizing beam-splitters (PBS) and variable neutral-density attenuators. We must use the attenuators because of other polarization modes, which cannot be muted by the half-wave plate and polarizing beam splitter system. For the best results, the power levels of the input signal states have to be as similar as possible. The power of the local oscillator was set to 10 μW.

The input signals are pair-wise interfered in Michelson interferometers. Each interferometer was made of a 50:50 beam-splitter (BS) and two plane mirrors attached to piezo crystals (PZT) controlling the phase shift of input signals. The piezo crystals were driven by the voltage source providing a triangle waveform with controlled amplitude 0-55 V and frequency 0.1-1.1 kHz. One output of each interferometer is brought to a 50:50 beam-splitter forming a Mach-Zehnder interferometer. This setup allowed us to prepare a coherent state, two mixed coherent states, and four mixed coherent states. The prepared states were interfered with the local oscillator and measured by the homodyne detector (HD), which was presented in 3. The interferences in the experiment are not perfect, but in theory, we assume the perfect interferences of coherent states. For this reason, the visibilities have to be as high as possible. The coherence length of the laser source is 10^{-4} m. For this reason, there are two delay lines (DL1, DL2) on adjustable stages in the setup for visibility as high as possible. The mirrors in the Michelson interferometers were on the adjustable stages too.
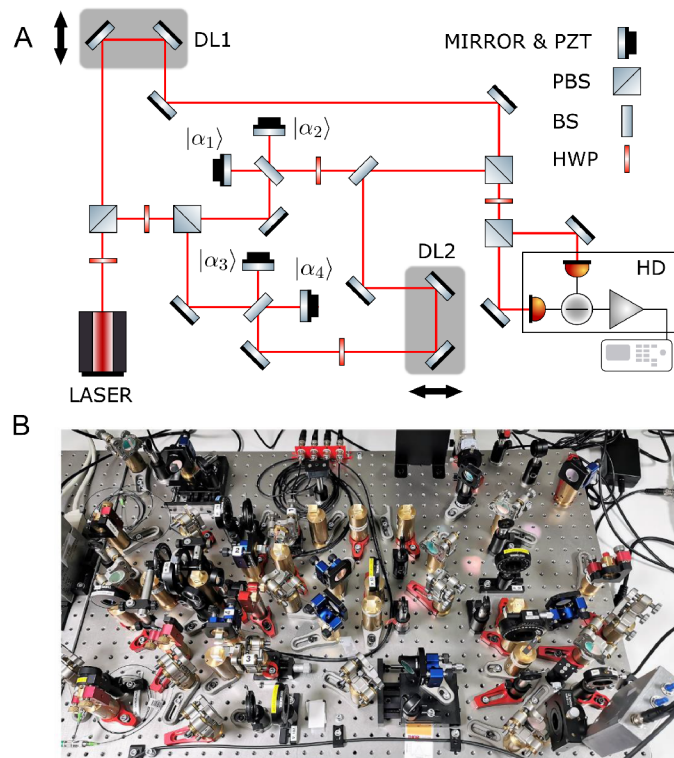
Figure 4.1: (A) The scheme of the experimental setup for the coherent state thermalization. (B) A photo of the experimental setup.

4.2 Transmittance and visibility characterization

The homodyne detector is placed and aligned at the output of the setup. However, the initial coherent states and the pairs of interfered coherent states are prepared after the attenuators and after Michelson interferometers, respectively. To properly characterize these states, we have to quantify the transmittance of optical paths between the detector and the point, where the states are prepared. In this goal, we measured the power of the laser signal at the input I_{in} and at the output I_{out} (homodyne detector input) of the optical setup for each path. From the measured powers we determined the transmittance $T = I_{\text{out}}/I_{\text{in}}$, which are listed in Table 4.1.

Table 4.1: Measured transmittances of individual signal paths.

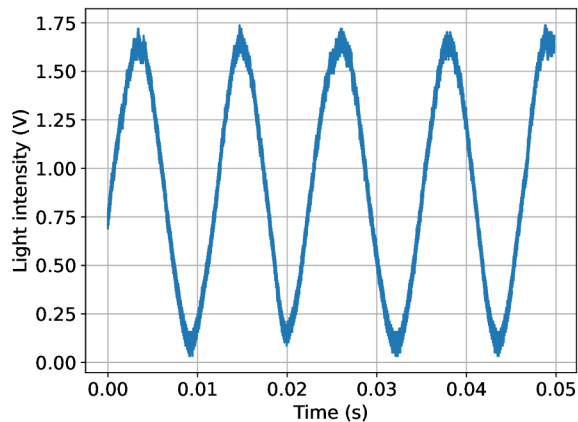| Signal path	T
$|\alpha_1\rangle$	0.178
$|\alpha_2\rangle$	0.159
$|\alpha_3\rangle$	0.175
$|\alpha_4\rangle$	0.167

Figure 4.2: The dependence of the signal intensity on the phase shift.

As said above, for the measurement of the coherent state thermalization we need to measure the visibilities of interferences. The visibilities depend on the setup adjustment and stability of the laser diode, thus they can slightly change in time. Hence, we have to determine them before the measurement. For this reason, we brought the laser signal from each interferometer to a high-sensitivity photodetector. The output was displayed on the oscilloscope. As we can see from Fig. 4.2, the measured function is sinusoidal with maximum I_{max} and minimum I_{max}. The visibility V of the interference is then given as

$$V = \frac{I_{\mathrm{max}} - I_{\mathrm{min}}}{I_{\mathrm{max}} + I_{\mathrm{min}}}. \tag{4.1}$$

The measured visibilities are listed in Table 4.2. As we can see, the visibilities of the coherent states $|\alpha_1\rangle + |\alpha_2\rangle$ and $|\alpha_3\rangle + |\alpha_4\rangle$ are larger than others. The reason is, that these interferences take place on the Michelson interferometers, which have much shorter arms and are more simple than other interferometers used in the setup.

Table 4.2: Measured visibilities of the interferences.

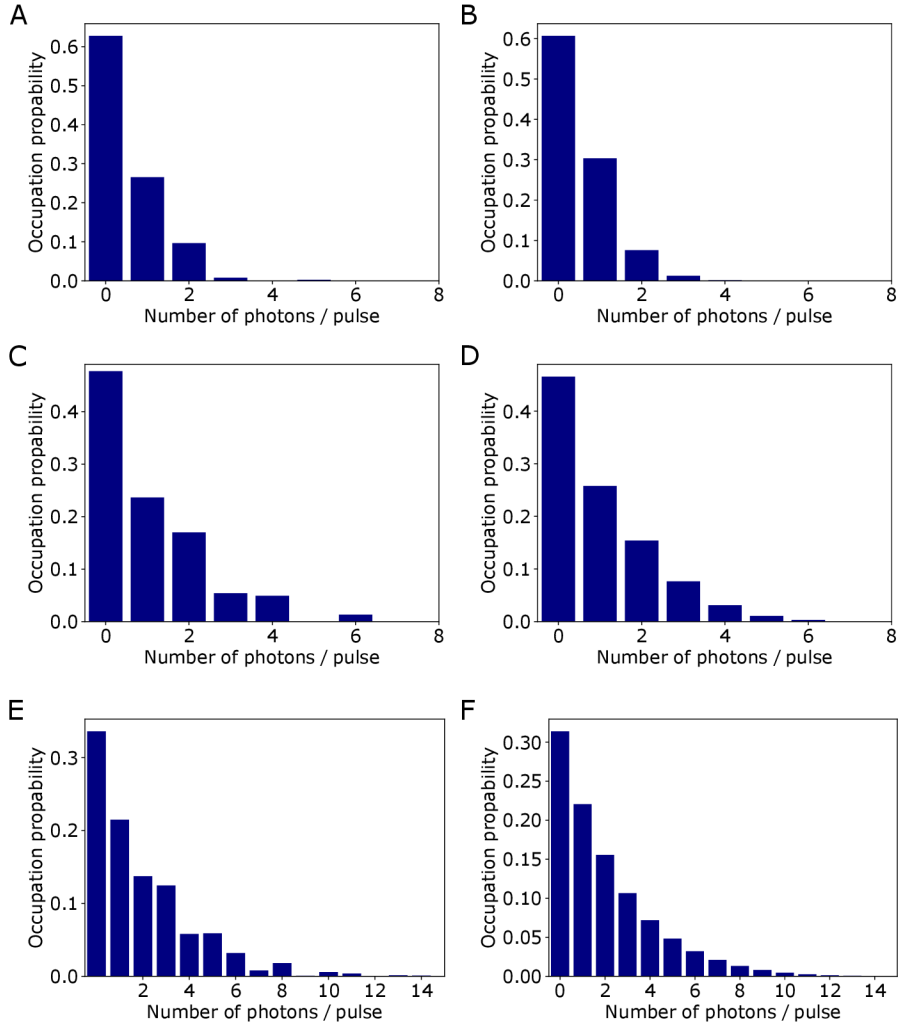| Interference	V
$|\alpha_1\rangle + |\alpha_2\rangle$	0.98
$|\alpha_2\rangle + |\alpha_3\rangle$	0.89
$|\alpha_3\rangle + |\alpha_4\rangle$	0.96
$|\alpha_2\rangle + LO$	0.91

Figure 4.3: Photon-number distribution of the initial coherent state (A-B) with input mean-photon number $\bar{n} = 2$, two interfered coherent states (C-D), and four interfered coherent states (E-F). Measured photon-number distributions are shown in the left panels (A, C, E). The corresponding ideal theoretical distributions are depicted in the right panels (B, D, F).

4.3 Coherent state thermalization results

For coherent state thermalization, we need to characterize the coherent state, 1st thermalization stage, and 2nd thermalization stage for several different mean photon numbers. For each state, we measured the photon-number distribution, its mean photon number $\bar{n}$, variance $\mathrm{Var}(n)$, and parameter $g^{(2)}$. The measured values are compared with the theoretical values, which are determined by numerical simulations. The coherent state is prepared from signal branch $|\alpha_2\rangle$, the 1st thermalization stage is prepared by mixing the two phase-randomized coherent states $|\alpha_1\rangle$ and $|\alpha_2\rangle$, and the 2nd stage thermalization is prepared by mixing all phase-randomized coherent states. The phase-randomization is done by the coprime frequencies of the drive signals of the piezo crystals. The comparison of the measured photon-number distributions with the theoretical ones for input mean photon number $\bar{n} = 2$ is shown in Fig. 4.3. The fidelity between measured and theoretical photon-number distributions is 0.994 for the coherent state, 0.982 for 1st thermalization stage, and 0.988 for 2nd thermalization stage.

The measured values of $\mathrm{Var}(n)$ and $g^{(2)}$ for mean values $\bar{n}$ are shown in Fig. 4.4. The measured data correspond well to theoretical values except for the $g^{(2)}$ values for low mean photon number ($\bar{n} \lesssim 1$). This is caused by the strong sensitivity of $g^{(2)}$ to noise in higher photon-numbers terms, which is unavoidable in experimental data. This sensitivity also increases the error bars. Furthermore, slightly larger values of $g^{(2)}$ compared to the theoretical value of $g^{(2)} = 1$ for initial coherent states represent another discrepancy in Fig. 4.4 B. It is caused by excess fluctuations of the coherent states, i.e. instabilities of the light source and instabilities of the balancing of the homodyne detection.
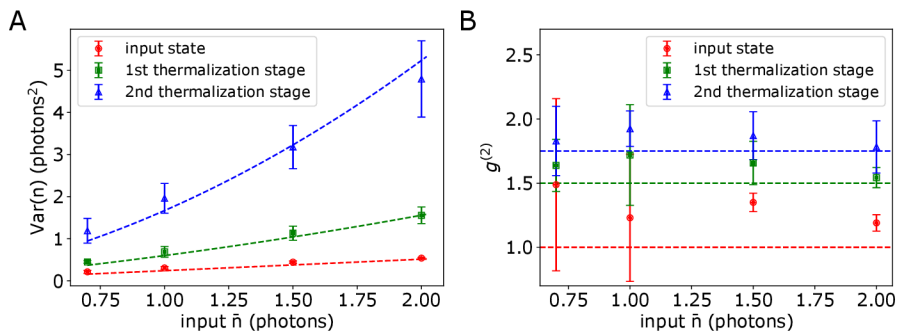

Figure 4.4: ((A) Variances of the measured photon statistics. (B) Values of the parameter $g^{(2)}$ calculated from the measured photon statistics. Points denote experimental data, dashed lines depict the ideal theoretical values.

Chapter 5

Conclusions and outlook

The main goal of this thesis was to characterize the quantum homodyne detector and describe the main problems associated with homodyne detection such as the selection of suitable photodiodes or balancing of the detector. We also showed how powerful tool the homodyne detection is for quantum states reconstruction. This was demonstrated in the coherent state thermalization experiment.

First, the methods used for the operation of the homodyne detector are discussed. In Section 3.1, the method for selection of the most suitable photodiodes is demonstrated. Furthermore, the dependence of the time responses on the bias voltage is shown. From the batch of 10 photodiodes, we choose the best-matching photodiodes. Then, in Section 3.2 the methods for balancing the homodyne detector are described and there is also shown the frequency spectrum of the unbalanced homodyne detector. The CMRR of the first peak in the electronic spectrum of the unbalanced homodyne detector is 45 dB. In Section 3.3, the measurement of the vacuum state is presented. From the measured data the quadratures are processed. From the quadrature statistics, the variance $\sigma^2 = 323$ and mean value $\mu = 21$ are determined. These values were used for the calibration of the homodyne detector. Also, we performed the measurement of the dependence of the variance of the vacuum state quadratures statistics on the local oscillator power. From this dependence, the suitable power of the local oscillator $10 \, \mu\text{W}$ was determined. The SNR at this power is higher than 20 dB.

In Sections 4.1 and 4.2, the basic properties of the optical setup, which is used for coherent state thermalization, are demonstrated. The main tasks of the setup adjustment and characterization are discussed, such as the transmittance and visibility measurements. Then, in Section 4.3, the results of the coherent state thermalization were provided. We prepared the coherent state, two mixed coherent states, and four mixed coherent states for four different input mean photon numbers. All states were measured with the homodyne detector. From the measured data, the photon number distributions were reconstructed via maximum likelihood estimation. Consequently, the variances of these distributions and $g^{(2)}$ parameters were determined and compared with theoretical values.

As the next step, we plan to study the thermalization process and its dynamic in more detail. We will place the heralding detectors at the unused output ports of the interferometers and study the thermalization conditioned on the non-detection (zero photons detected) of these detectors. Furthermore,

we will continue the development of the homodyne detectors. We aim for a homodyne detector with a bandwidth large enough for detecting the signal from an ultra-fast mode-locked laser. Another goal is to improve the signal-to-noise ratio and balancing of our detectors.

Bibliography

[1] R. Lange and B. Smutny. Homodyne BPSK-based optical inter-satellite communication links. In Steve Mecherle and Olga Korotkova, editors, *Free-Space Laser Communication Technologies XIX and Atmospheric Propagation of Electromagnetic Waves*, volume 6457, page 645703. International Society for Optics and Photonics, SPIE, 2007.

[2] B. J. Puttnam et al. Self-homodyne detection in optical communication systems. *Photonics*, 1(2):110–130, 2014.

[3] W. Wells, R. Stone, and E. Miles. Secure communications by optical homodyne. *IEEE Journal on Selected Areas in Communications*, 11(5):770–777, 1993.

[4] The LIGO Scientific Collaboration. Enhanced sensitivity of the LIGO gravitational wave detector by using squeezed states of light. *Nature Photonics*, 7(8):613–619, 2013.

[5] D. T. Smithey, M. Beck, M. G. Raymer, and A. Faridani. Measurement of the wigner distribution and the density matrix of a light mode using optical homodyne tomography: Application to squeezed states and the vacuum. *Phys. Rev. Lett.*, 70:1244–1247, 1993.

[6] H. Hansen, T. Aichele, C. Hettich, P. Lodahl, A. I. Lvovsky, J. Mlynek, and S. Schiller. Ultrasensitive pulsed, balanced homodyne detector: application to time-domain quantum measurements. *Opt. Lett.*, 26(21):1714–1716, 2001.

[7] G. Breitenbach, S. Schiller, and J. Mlynek. Measurement of the quantum states of squeezed light. *Nature*, 387:471–475, 1997.

[8] A. I. Lvovsky, H. Hansen, T. Aichele, O. Benson, J. Mlynek, and S. Schiller. Quantum state reconstruction of the single-photon fock state. *Phys. Rev. Lett.*, 87:050402, 2001.

[9] E. Jakeman, C.J. Oliver, and E.R. Pike. Optical homodyne detection. *Advances in Physics*, 24(3):349–405, 1975.

[10] R. Okubo, M. Hirano, Y. Zhang, and T. Hirano. Pulse-resolved measurement of quadrature phase amplitudes of squeezed pulse trains at a repetition rate of 76 mhz. *Opt. Lett.*, 33(13):1458–1460, 2008.

[11] O. Haderka, V. Michálek, V. Urbášek, and M. Ježek. Fast time-domain balanced homodyne detection of light. *Appl. Opt.*, 48(15):2884–2889, 2009.

[12] A. Zavatta, M. Bellini, P. L. Ramazza, F. Marin, and F. T. Arecchi. Time-domain analysis of quantum states of light: noise characterization and homodyne tomography. *J. Opt. Soc. Am. B*, 19(5):1189–1194, 2002.

[13] R. Kumar, E. Barrios, A. MacRae, E. Cairns, E.H. Huntington, and A.I. Lvovsky. Versatile wideband balanced detector for quantum optical homodyne tomography. *Optics Communications*, 285(24):5259–5267, 2012.

[14] M. Cooper, C. Söller, and B. J. Smith. High-stability time-domain balanced homodyne detector for ultrafast optical pulse applications. *Journal of Modern Optics*, 60(8):611–616, 2013.

[15] A. I. Lvovsky and M. G. Raymer. Continuous-variable optical quantum-state tomography. *Rev. Mod. Phys.*, 81:299–332, 2009.

[16] Z. Hradil. Quantum-state estimation. *Physical Review A*, 55(3):R1561–R1564, 1997.

[17] A. I. Lvovsky. Iterative maximum-likelihood reconstruction in quantum homodyne tomography. *Journal of Optics B: Quantum and Semiclassical Optics*, 6(6):S556, 2004.

[18] M. Ježek, J. Fiurášek, and Z.Hradil. Quantum inference of states and processes. *Physical Review A*, 68(1), 2003.